Seismic array detection of subducted oceanic crust in the lower mantle

Sebastian Rost,[1] Edward J. Garnero,[2] and Quentin Williams[3]

[1]   We analyze short-period precursory energy to *PP* that can be observed in seismograms in the distance range from $\sim$95° to 105° to infer the behavior of subducted slabs beneath western Pacific subduction zones. *PP* is a *P* wave once reflected at the free surface between the source and receiver. Using high-resolution seismic array techniques, we analyze the incidence angle, timing, and azimuth of the *PP* precursors. The precursory energy is resolved to originate from off great circle path azimuths and is consistent with scattering by small-scale heterogeneities. Assuming single scattering, upper mantle- and midmantle-derived scatterer locations show a strong geographical and depth correlation to high seismic velocities in tomographic studies. Scattering locations beneath the Tonga and Mariana subduction zones outline continuous dipping structures to a depth of at least 1000 km, consistent with scattering associated with subducted former oceanic lithosphere. Scatterer locations uniquely explain the timing, slowness, and back azimuth of the *PP* precursors at the array. The observed reflections can be explained with the velocity impedance variations expected for high-pressure basalt juxtaposed with pyrolite or harzburgite and thus may be due to the paleo-Mohorovičić discontinuity within subducted slabs. These results are consistent with basaltic crust penetrating into the lower mantle. This method provides a means for tracking the location of geochemically enriched former oceanic crust in the lower mantle by using recordings of globally distributed seismic arrays and is complementary to longer-wavelength constraints on high seismic velocity slabs inferred from tomography.

1.   Introduction

[2]   The nature of subducted oceanic lithosphere, or "slabs," has been actively researched for over 4 decades; deep slab morphology is indirectly inferred from tomographically derived seismic velocities which suggest a range of behaviors including slab stagnation in the mantle transition zone, horizontal deflection by the 660 km phase transition, and penetration into the lower mantle perhaps even to the core-mantle boundary [e.g., *Engdahl*, 1995; *Lay*, 1994; *Gorbatov et al.*, 2000; *Fukao et al.*, 2001]. Such tomographic images do not, however, constrain the fate of the geochemically enriched basaltic oceanic crust, which might detach from the underlying lithospheric mantle [*Irifune and Ringwood*, 1993; *Christensen and Hofmann*, 1994; *Karato*, 1997; *Kubo et al.*, 2002; *Lee and Chen*, 2007]. Indeed, oceanic crust is typically <7 km thick and hence far below the resolution of current tomographic analyses. Additional information, such as high-resolution waveform analyses, is thus needed to supplement the somewhat long-wavelength, tomographically derived images of subducting slabs.

[3]   It is widely accepted that cold dense slabs are a major driving force of convection in the Earth's mantle and the configuration of subducting slabs in the mantle can give strong constraints on the evolution of mantle flow [*van Keken et al.*, 2002]. The depth dependence of mixing associated with mantle convection, however, is still debated. Geochemical studies have often favored layered convection with a reservoir at a depth that is geochemically more primitive than the upper mantle. The inferred volume of this reservoir indicates that it may lie at depths at or below 660 km, i.e., within the lower mantle [*Silver et al.*, 1988; *Workman and Hart*, 2005]. The possible preservation of such a layer has been attributed to the convection-inhibiting nature of the 660 km discontinuity, owing to the endothermic phase transition and viscosity increase at this depth [e.g., *Lambeck and Johnston*, 1998]. Nonetheless, subducting enriched oceanic crust can supply the deep mantle with enriched material for such a reservoir [*Coltice and Ricard*, 1999]; conversely, pervasive deep subduction of both enriched crust and its underlying depleted mantle would be anticipated to drive mixing and resultant mantle homog-

[1]School of Earth and Environment, Institute of Geophysics and Tectonics, University of Leeds, Leeds, UK.
[2]School of Earth and Space Exploration, Arizona State University, Tempe, Arizona, USA.
[3]Department of Earth Sciences, University of California, Santa Cruz, California, USA.
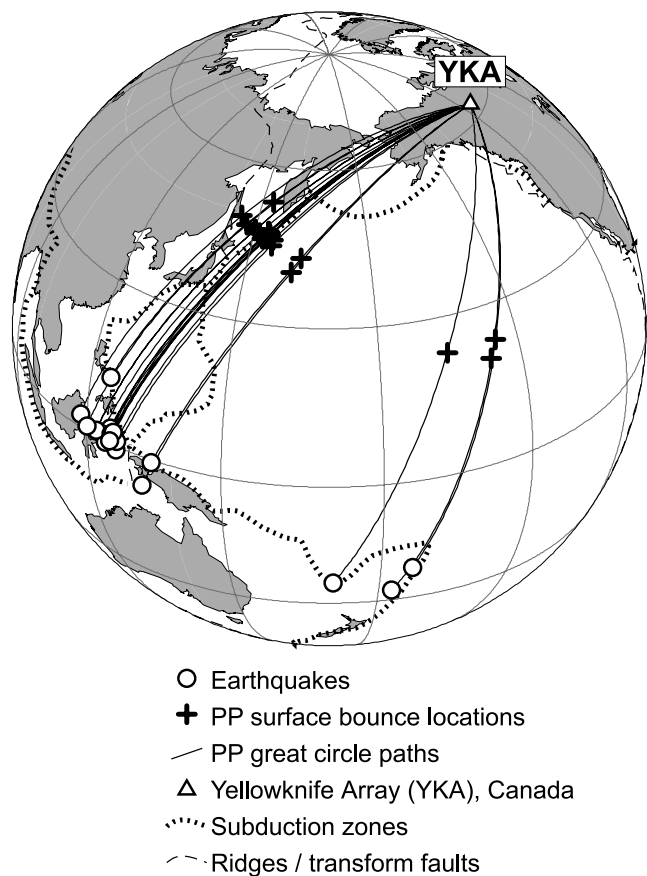
enization [*Meibom and Anderson*, 2004]. Indeed, seismic tomography provides evidence for planar high-velocity features extending well into the lower mantle beneath past or present subduction zones [*van der Hilst et al.*, 1997; *Grand*, 2002], supporting whole mantle convection. Numerical geodynamical studies have produced results consistent with both end-members of mantle convection as well as alternation between the two regimes [*Christensen and Yuen*, 1984; *Tackley et al.*, 1993]. The fate of the basaltic crust associated with the slab is, however, ill resolved by tomographic techniques, and it has been proposed that it may delaminate or be concentrated near 660 km [*Irifune and Ringwood*, 1993; *Karato*, 1997; *Lee and Chen*, 2007]. Quantification of the transfer of geochemically enriched crust between the upper and lower mantle thus requires additional and independent information.

[4] Here, we describe a seismic array approach to studying deep heterogeneities in and beneath subduction zones. Traditional short-period seismic array data are used that have sensitivity to short-scale (e.g., tens to hundreds of kilometers) structure and are hence ideally suited to investigate the possible connection between deep, short-wavelength compositional heterogeneities and subduction processes.

2. Method

[5] To study this problem, we investigate seismic recordings from the small-aperture Yellowknife Array (YKA) in northern Canada. YKA consists of 18 short-period ($\sim$1 Hz) vertical stations deployed along two perpendicular lines (in a N-S orientation) each 20 km long with an interstation spacing of $\sim$2.5 km. YKA has been designed to detect high-frequency P waves from underground nuclear explosions [*Manchee and Weichert*, 1968] and is, therefore, well suited to the study of the scattered waves targeted here. Array methods are used to study 21 strong earthquakes in the southwest Pacific region (Figure 1). The events were selected from a larger data set of about 160 events recorded from 1989 to 1996. We selected events with impulsive onsets of the PP waveforms in the raw seismograms to ensure accurate measurement of differential traveltimes between PP and any precursors. Additionally, we selected events showing strong and impulsive precursors to PP which are not masked by extensive P or P_{diff} coda. Epicentral distances from these earthquakes range from 95° to 105° (Figure 1). Information describing these events is given in Table S1 in the auxiliary material.[1] We restrict our search to shallow earthquakes to avoid interference between depth phases from deep or intermediate-depth earthquakes and the scattered energy of interest. Deep earthquakes would show less scattering from the source region than the shallow events used here, but we do not expect this source scattering to arrive in the time window in which the PP precursors are observed. Therefore, we do not think that restricting this study to shallow earthquakes is particularly restrictive.

[6] We investigate the wavefield of the seismic phase PP as well as energy in a few hundred second time window leading up to PP. An example earthquake is shown in

---

○ Earthquakes
+ PP surface bounce locations
⌒ PP great circle paths
△ Yellowknife Array (YKA), Canada
⋯ Subduction zones
⌒ Ridges / transform faults

Figure 1. Earthquake and seismic array geometry for the *PP* data used in this study. Earthquakes in the southwest Pacific span an epicentral distance range of $\sim$95°–105°, with *PP* surface bounce point locations in the central and northwestern Pacific.

Figure 2 along with a fourth-root slant stack (vespagram) [*Davies et al.*, 1971; *Muirhead and Datt*, 1976]. The vespagram process analyzes the energy content of the incoming seismic signals as a function of lateral incidence angle (back azimuth, which is held constant) and vertical incidence angle (slowness). The slowness is the inverse phase velocity of signals traveling across the array and helps to identify the arrivals of different seismic phases. The energy is mapped in time-slowness space. Figure 3 shows raw data for the event of 12 July 1995 along with energy as a function of slowness and back azimuth in six consecutive time windows, each 50 s long. The first three time windows show the P_{diff} arrival and its decaying coda. The fourth time window shows the total decay of the P_{diff} coda and the presence of uncorrelated noise. The fifth time window, however, shows coherent energy with a slowness larger than that of P_{diff} and arriving off great circle path and is, therefore, likely unrelated to P_{diff}. The final (sixth) time window contains the PP arrival and displays the peak beam power with higher slowness than the energy detected in the fifth time window, as expected for PP. The energy in the fifth time window, i.e., PP precursors, has been noted previously in stacks of seismic array data [*Rost et al.*, 2006] and is only observed in the short-period wavefield [*Earle*, 1999].

[7] Figure 4 shows a beam trace for *PP* slowness for the event shown in Figure 2, which also shows the decay of P_{diff} coda and the gradual increase of energy toward the *PP* arrival. Energy preceding *PP* (denoted *P*P*) is clearly

(a) Raw data (02 Apr 1996 18:50; Δ=100.14 deg)

(b) Vespagram

(c) Vespagram Zoom

visible in Figures 2–4, generally with slownesses smaller than *PP* and larger than P_{diff} and with amplitudes well above the background noise level. This suggests a surface origin for the reflection location of *P*P* on the source side of the *PP* surface reflection point; otherwise, *P*P* slownesses would be larger than *PP*. For asymmetric paths and scattering at depths this no longer holds true, and origins from both sides of the *PP* surface reflection points are possible. No major seismic arrivals are predicted for the time window immediately preceding *PP* in the distance range of our observations; thus, the precursors are unexpected. *PP* underside reflections off the upper mantle discontinuities arrive earlier in the seismogram [*Flanagan and Shearer*, 1999], and although these have been detected in short-period array data [*Rost and Weber*, 2002], they are not clearly observable in this data set. Reduced *P*P* slownesses rule out an origin close to *PP* surface bounce points, or slownesses would be nearly identical to *PP* slowness (Figure 5a). Isolated observations of asymmetric *PP* precursors (Figure 5b) have been previously noted and can possess substantial amplitudes due to focusing from upper mantle velocity structure [*Wright*, 1972; *King et al.*, 1975]. Nonetheless, it is found that these precursors originate from scattering or reflection off dipped surfaces at or near the surface of the Earth.

[8] We detect 110 *P*P* precursors from vespagrams of our selected 21 events and measure the complete slowness vector, defined by slowness (vertical incidence angle) and back azimuth (horizontal incidence angle), using a frequency–wave number (*fk*) analysis [*Capon*, 1973] on each precursor arrival. Although the slowness vector, in general, is 3-D, the lack of topography of YKA allows us to describe it through slowness and back azimuth, i.e., as a 2-D vector. The frequency band studied in the *fk* analysis spans from 0.5 to 1.4 Hz. This frequency band lies well within the flat instrument response of the YKA instrumentation and has been found in earlier studies [e.g., *Rost and Weber*, 2002] to be a good frequency band for maximizing the signal-to-noise ratio. We only study precursors with impulsive onsets and reject energy with emergent onsets or those having a more continuous or ringing nature since incidence angles might change along the wavelet. Short time windows of typically 4 to 6 s were used in the *fk* analysis. The short time windows help to get
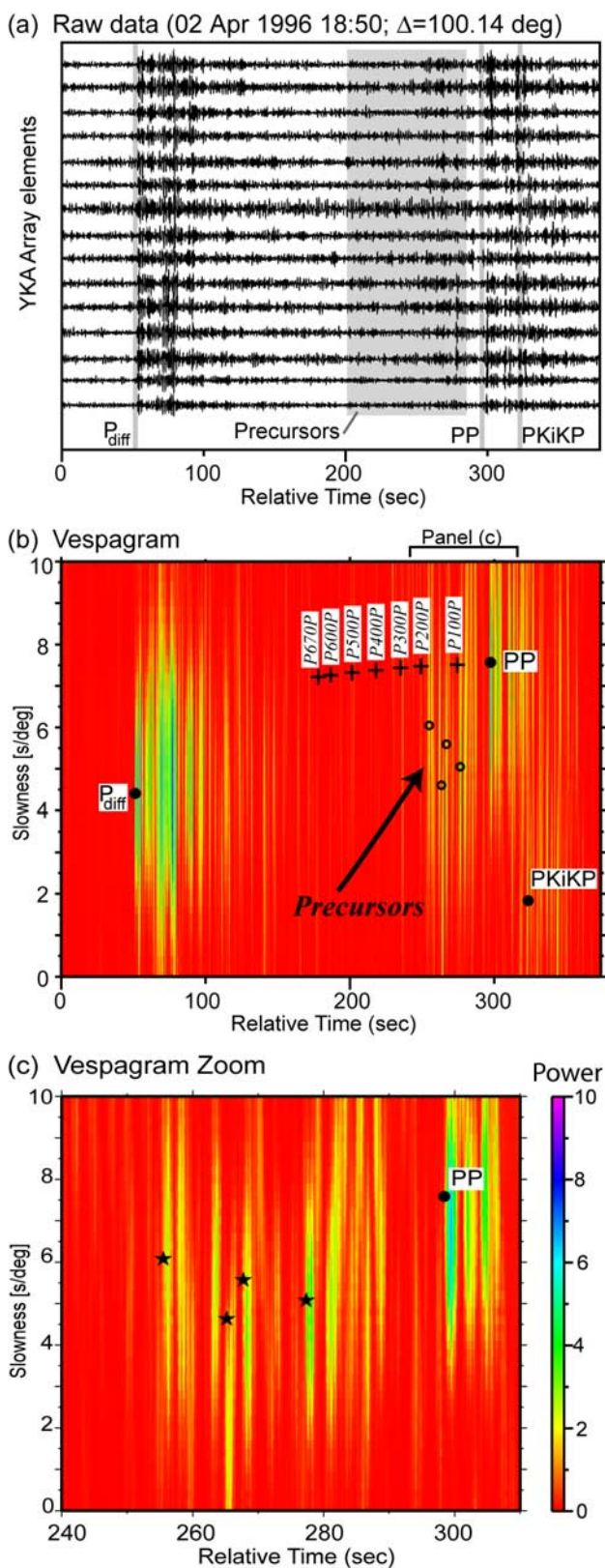
Figure 2. (a) Raw seismograms for an earthquake on 2 April 1996 (source depth is 41 km, epicentral distance is 100.14°) showing the time window that includes P_{diff} to *PKiKP*. Each trace corresponds to a different YKA station. The shaded region indicates the time window where the raw data show enhanced energy preceding *PP*. (b) Vespagram of the earthquake in Figure 2a. Crosses indicate the theoretical slowness-time values for possible underside reflections from depths of 100, 220, 300, 400, 500, 600, and 670 km (noted *P100P*, *P200P*, etc.), occurring at the *PP* path midpoint. Note the distinguishably different slownesses of the midpoint reflection predictions from those computed for the observed precursors analyzed here (open circles). (c) A zoom into the *PP* precursor time window. Four *P*P* precursors are detected (stars) with slownesses smaller than *PP* but larger than P_{diff}.
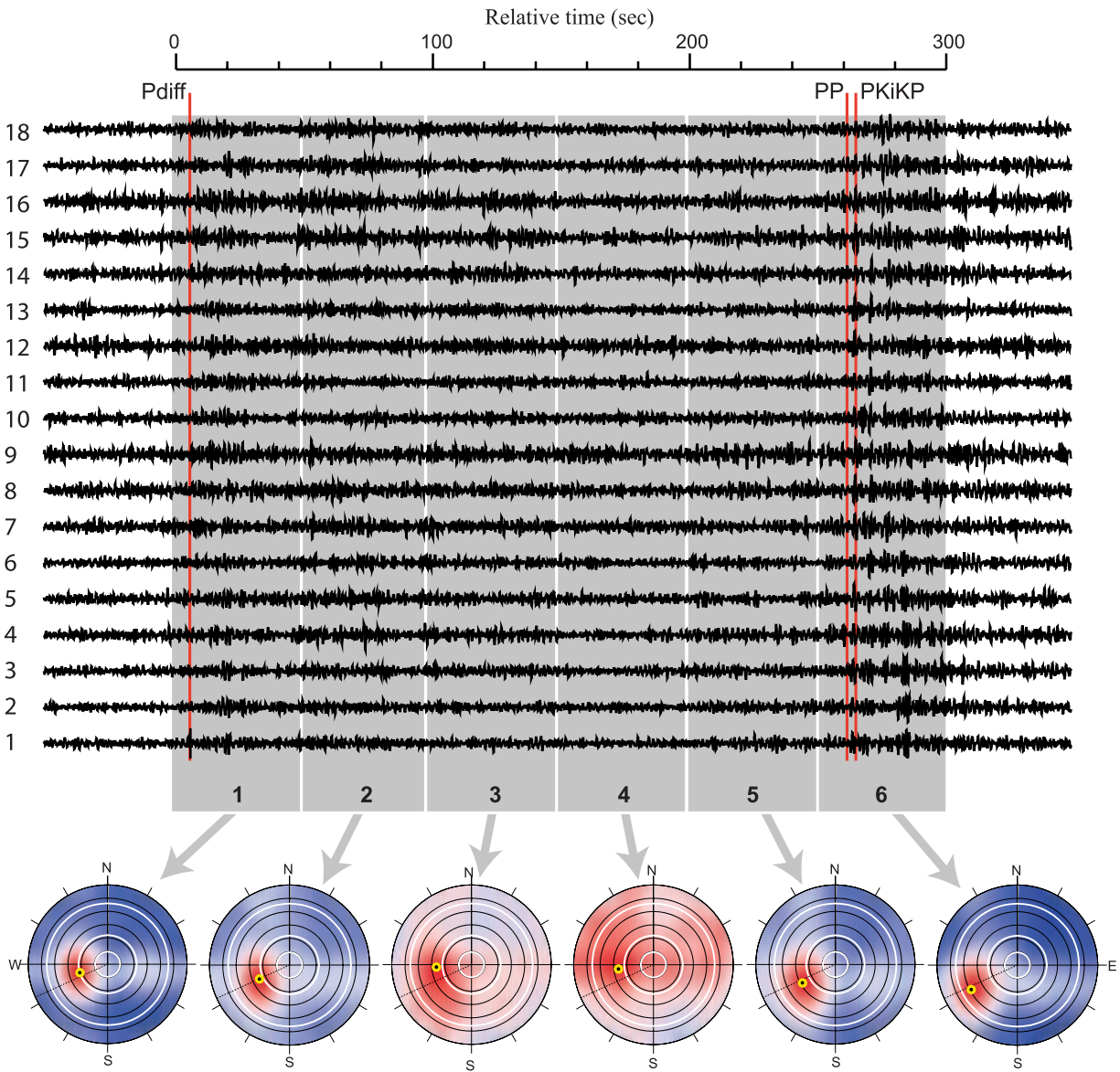
Figure 3. Raw YKA recordings for the event on 12 July 1995 (distance is 103.57, depth is 11 km, back azimuth is 245.8) are shown. Amplitudes are normalized by the maximum amplitude of the trace. Six time windows are highlighted by gray boxes, for which back azimuth and slownesses were calculated using a time domain stacking technique and shown in polar plots beneath the traces. Angle (clockwise) corresponds to back azimuth from the array, and distance from the center corresponds to slowness from 0 s/deg at the center to 12 s/deg along the circumference. Beam power for varying slowness and back azimuth for these time windows is shown (red is strongest; blue is weakest), with the highest values indicated by the yellow circles with black centers. The thin dashed line in each polar plot is the great circle path back azimuth. White circles correspond to slowness predictions of 1.9 s/deg, 4.4 s/deg, and 9.2 s/deg. The polar plot for the first time window shows the P_{diff} arrival coming in near predicted values (i.e., CMB slowness of ~4.4 s/deg), similar to PP (sixth time window). Intermediate windows, however, show evidence for off great circle path energy and correspond to precursors modeled here.

exact measurements of the incidence energy and are long enough for the wavelets to travel across the array for the slownesses of interest. When necessary, time window locations were adjusted to prevent inclusion of multiple precursor arrivals in the *fk* analysis; this avoids averaging slownesses and back azimuths of multiple arrivals.

[9] For each arrival we obtain slowness, back azimuth, and differential traveltime information. This enables us to use a backprojection of the scattered energy to a unique scattering location in the Earth [*Weber and Wicks*, 1996] using ray tracing (Figure 5) through a one-dimensional velocity model [*Kennett and Engdahl*, 1991]. The slowness resolution of YKA for the typical signal-to-noise ratio found

(a) PP beam

(b) Envelope of PP beam
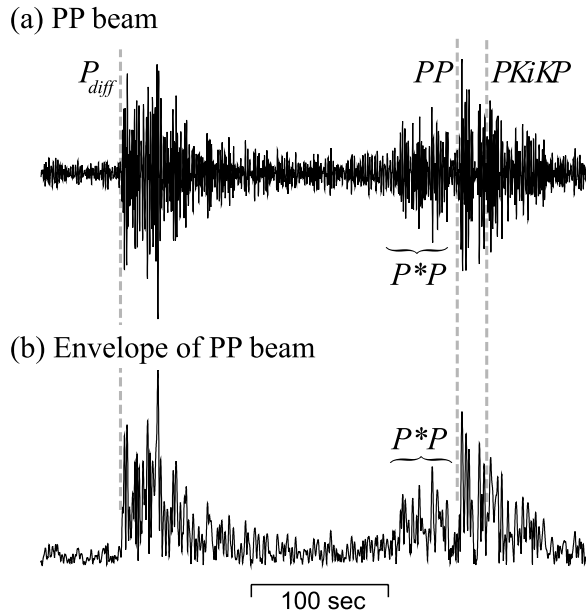
Figure 4. (a) The YKA array beam trace for the PP slowness and back azimuth for the event shown in Figure 2. Arrival times for P_{diff}, PP, and the inner core reflection $PKiKP$ are marked. (b) The envelope of the beam trace shown in Figure 4a. Note the increase of energy starting about 40 s before PP, which are the $P*P$ arrivals investigated here.

in the data is about ±0.2 s/deg, and the back azimuth resolution is about ±5°. Traveltimes were picked by hand in high-resolution fourth-root vespagrams [*Davies et al.*, 1971; *Muirhead and Datt*, 1976], while slowness and back azimuth were picked in vespagrams and through *fk* analysis of short time windows [*Capon*, 1973]. Traveltimes were deemed to be accurate to within 0.2 s. These measurement uncertainties allow us to estimate the mislocation of the scatterers from our back-tracing algorithm. We find that with the maximum uncertainties, we are able to locate the scatterer within 90 km (i.e., <1° at the surface). The traveltime uncertainty only has a minor impact on the location of the scatterer, with the back azimuth uncertainty having the biggest effect on the scatterer location. Using larger arrays with better slowness and back azimuth resolution would decrease the mislocation of the scatterer even further.
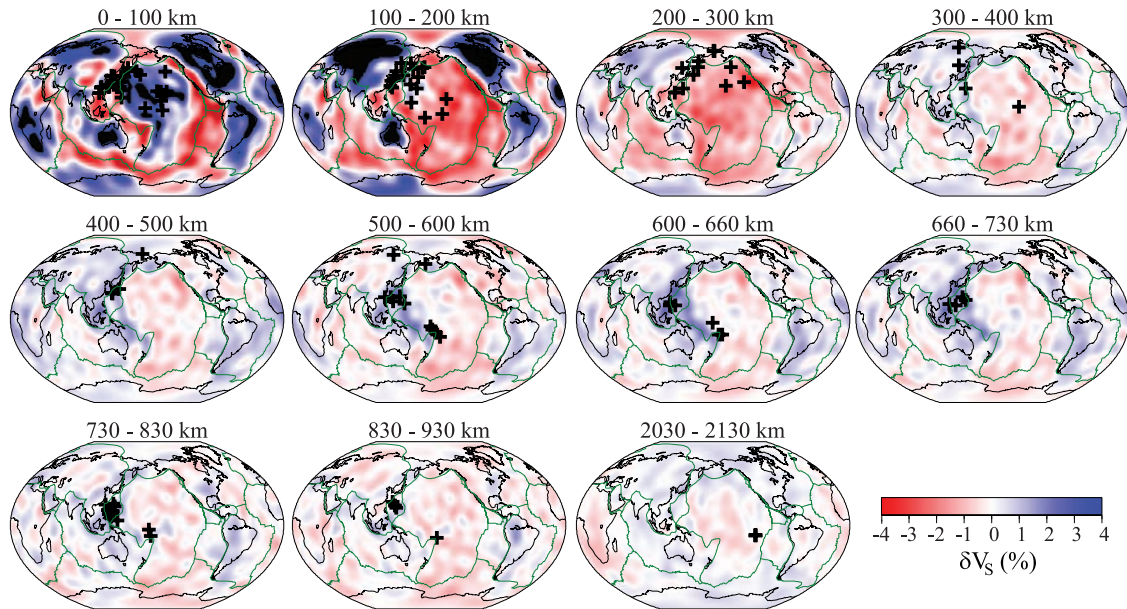
[10] We explored a variety of scattering mechanisms to find a solution for slowness, back azimuth, and traveltime for each precursor. Tested scattering mechanisms include $P*P$, $S*P$, $P*PP$, and $PP*P$. We find that only $P*P$ scattering uniquely explains the combination of slowness, back azimuth, and traveltime for our observations. This indicates forward scattering of the P wave energy from small-scale heterogeneities along the raypath.

3. Results

[11] The mapped scatterer locations are compared to a global S wave tomographic model [*Ritsema and van Heijst*, 2000] in Figure 6a and a global P wave velocity model
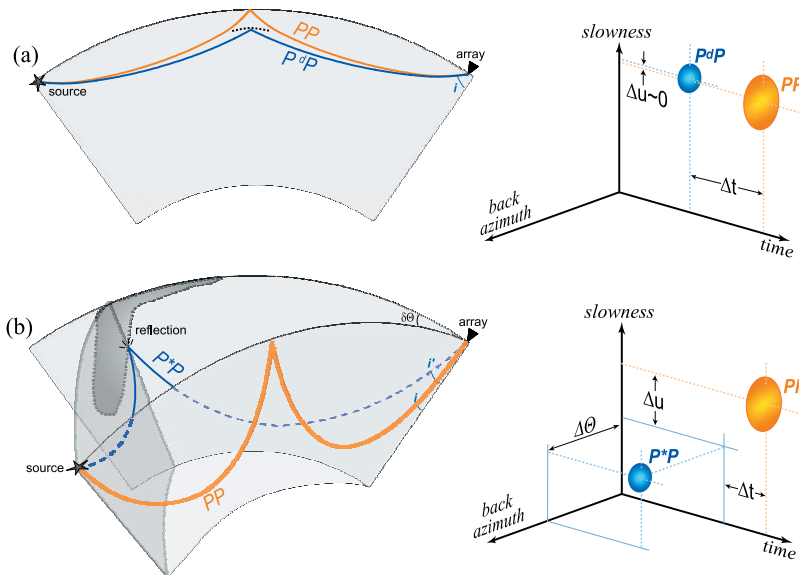

Figure 5.   (a) Symmetric underside reflections (P^dP) from upper mantle discontinuities will produce precursors to PP with similar incident angles i and hence similar slownesses. For example, the slowness differences between PP and underside reflections off the 410 and 660 km discontinuities are 0.2 and 0.4 s/deg, respectively, for the IASP91 model [*Kennett and Engdahl*, 1991] and 90° epicentral distance. Shallower reflectors produce an even smaller differential slowness, which is not resolvable. (b) Sketch of the back-tracing algorithm for a specific source which utilizes the *fk* analysis derived difference in incidence angles of PP and $P*P$ (from the differential slowness, Δu), the $PP-P*P$ differential time, and the differential back azimuth $\Delta\Theta$ information. $P*P$ is thus commonly born from reflections involving wave paths well out of the great circle plane.

(a) Imaged scatters and δV_S heterogeneities
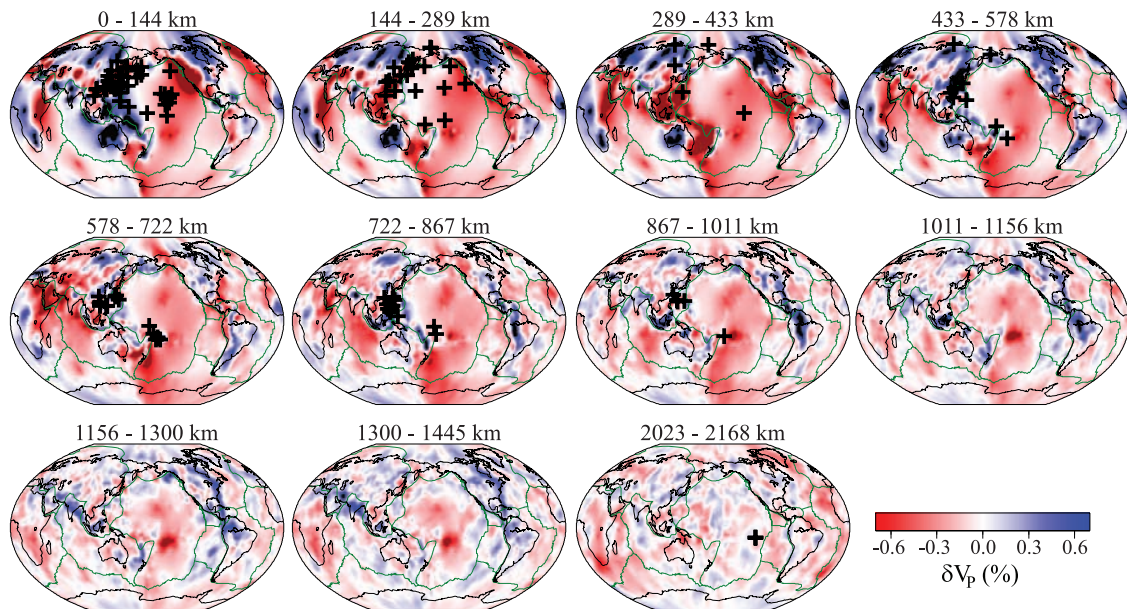
Figure 6. (a) Map view of scatterer locations (crosses) determined from *P*P* arrivals. Results are shown in different depth slices down to 930 km depth and in one deeper depth shell (2030–2130 km) where two isolated scatters where mapped. Depth ranges are shown at the top of each globe. For comparison, shear wave velocity perturbations as imaged by tomography are also shown in each depth shell using model S20RTS [*Ritsema and van Heijst*, 2000]. High seismic velocities are shown in blue and low velocities in red. Green lines show approximate plate boundaries. (b) Same as in Figure 6a but showing tomographically derived *P* wave velocity perturbations [*Kárason and van der Hilst*, 2001]. Depth slice thicknesses differ between Figures 6a and 6b owing to differences in layer parameterization in original models.

[*Kárason and van der Hilst*, 2001] in Figure 6b. Many precursors are mapped into scatterer locations in the upper mantle above 410 km, but about half of all detections are located in the mantle transition zone (410–600 km depth) or in the lower mantle down to depths of ~1000 km (Figure 7).

Two detections originate about 700 km above the core-mantle boundary (CMB), near 2100 km depth, which are from different earthquakes (12 July 1995 and 13 December 1993). The shallowest scatterers (e.g., above 300 km depth) have been described previously [*Wright*, 1972; *Weber and*
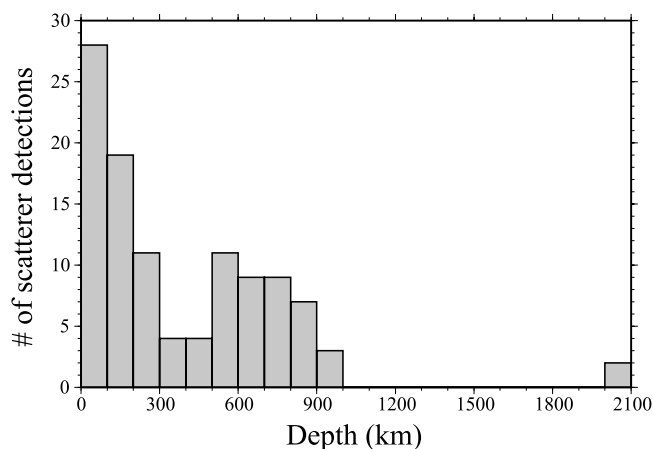
**Figure 7.** Histogram of scatterer depths imaged in this study.

Wicks, 1996] and can be explained by small-scale heterogeneities in the lithosphere and upper mantle. Wave paths are steeply incident upon mapped scattering surfaces (Figure 8), and most scatterers are relatively close to theoretical great circle paths. In this study, we do not distinguish between a scatterer and a reflection off of a contiguous interface (dipping or otherwise). We simply assume that the minimum scale of scatterers or reflectors is of the order of the seismic wavelength which, for our short-period P wave energy, is roughly between 8 and 12 km in the depth range of $100–1000$ km, respectively. Therefore, we likely observe forward scattering of the PP wavefield [*Aki and Richards*, 1980; *Wu and Aki*, 1988]. A full description of the nature of the scattering responsible for our observations is difficult. We do not have strong constraints on amplitude information of $P*P$, in part owing to the array processing and in part because of the amplitudes of the reference phase, PP, being dependent on factors that are not well known between observations, such as crustal multiples near the PP bounce point.

[12] The waveforms of precursors do not exhibit clear consistency with PP in waveshape or polarity (Figure 9). Some, however, are similar to direct P and thus do not appear to have the 90° phase shift, i.e., a Hilbert transform, as PP from an underside reflection [*Richards*, 1972]. Modeling these waveforms requires computation of synthetic seismograms for 3-D wavefield propagation at high frequency, which is not only beyond the scope of this paper but also not yet feasible for the epicentral distances and high frequencies used here. However, while it is not possible to fully resolve the issue of whether we observe isolated scatterers (e.g., compositional blobs) as opposed to layering or contiguous heterogeneities (e.g., slab-like features), we note that the waveform variability of the precursors may be indicative of heterogeneities of different scales and/or shapes.

[13] The scatterer locations beneath 400 km depth appear well correlated with surface regions possessing past or present subduction. They are also within or near to tomographically derived high seismic velocities in the lower mantle in the western Pacific, especially beneath the Marianas and Tonga subduction zones (see Figures S1–S3 and

Animation S1 in the auxiliary material for more detail). The apparently continuous high seismic velocities beneath subduction zones as seen in tomographic models have been used to argue for subducted slabs entering the lower mantle and descending to deeper depths [e.g., *van der Hilst et al.*, 1991; *Grand et al.*, 1997; *van der Hilst et al.*, 1997; *Fukao et al.*, 2001; *Grand*, 2002]. The comparison with tomographic cross sections (e.g., Figure 6 and auxiliary material Figures S2 and S3) shows that most $P*P$ scattering points at depth are located at or very close to boundaries between high- and low-velocity regions of the midmantle, providing independent support for slab penetration into the shallow

(a) Scatterer locations and angles: above 670 km depth
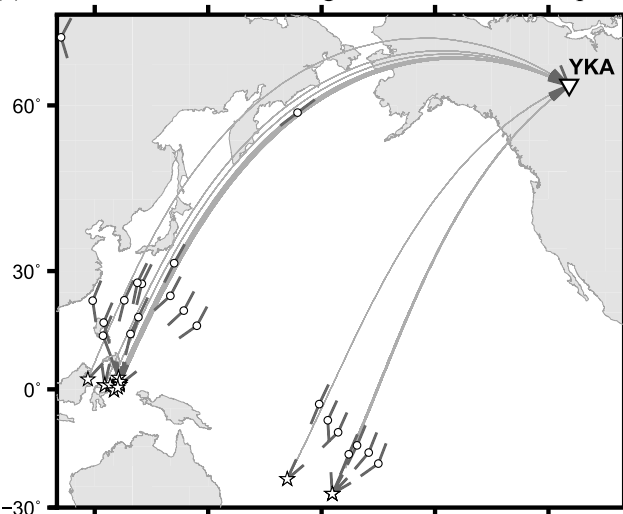
(b) Scatterer locations and angles: below 670 km depth
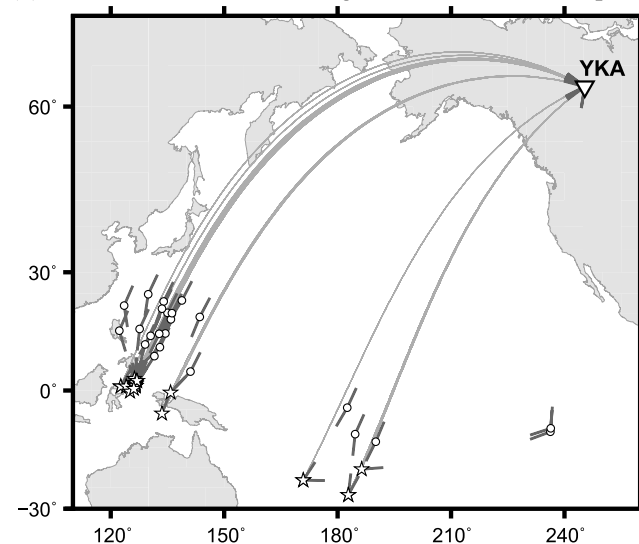
Figure 8. (a) Scatterers at 670 km depth and (b) scatterers below 670 km depth. Earthquake sources (stars), the Yellowknife Array (YKA, inverted triangle), and great circle paths (gray lines between sources and YKA) are shown along with scatterer locations (open circles). Short, thick gray lines at scatterers indicate the scatterer angles at each reflection location; short gray lines at sources and YKA show azimuth and back azimuth, respectively, to reflection locations.
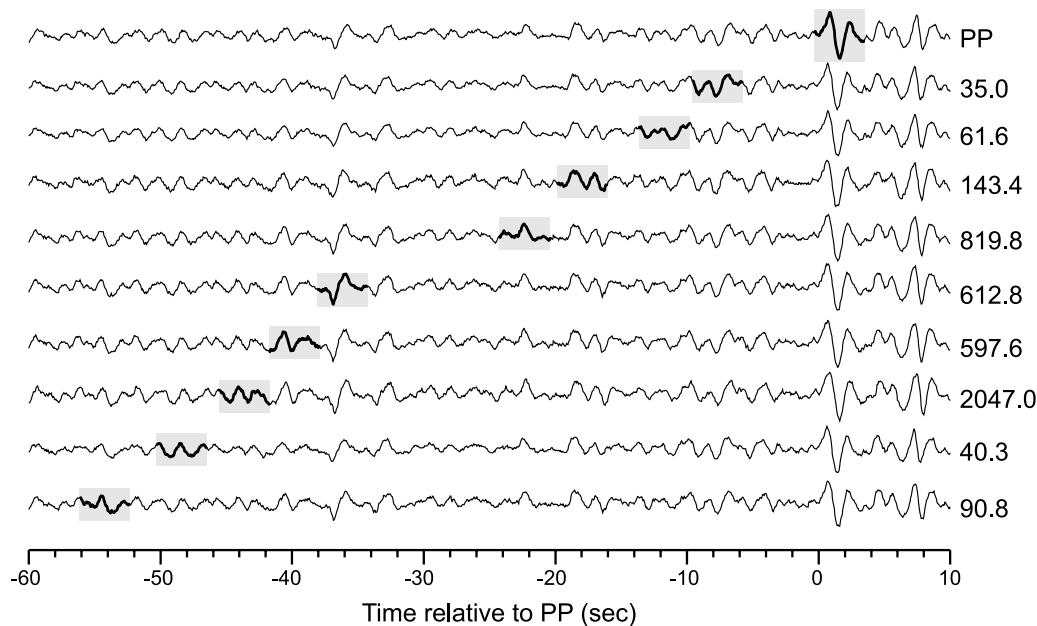
Figure 9. Beam traces constructed for the slowness and back azimuth calculated for each individual precursor are shown. Traces are for the 12 July 1995 event. The identification of each precursor is first determined in the vespagram, and then beams were formed. The *PP* wavelet is shown in the top trace and is underlain by traces for precursors progressively further in front of *PP*. Mapped precursor depths are indicated on the right.

and middle lower mantle. For the Marianas subduction zone, scatterer locations are in good agreement with high velocities from tomography, inferred slab configurations from seismicity-constructed Wadati-Benioff zones (see auxiliary material Figure S3a), as well as recent slab reconstructions [*Miller et al.*, 2004]. Moreover, seismic wave dispersion, multipathing, and converted seismic phases along the strike of the Tonga slab indicate that a high-velocity crustal-scale feature persists to ~450 km in depth in this region [*Gubbins et al.*, 1994]. Previous detections of reflections in or near this region that may be subduction related include a region of reflectors deeper than 1000 km to the northeast of our Marianas region (auxiliary material Figure S1) [*Kaneshima and Helffrich*, 1999; *Castle and Creager*, 1999; *Krüger et al.*, 2001; *Niu et al.*, 2003; *Kaneshima and Helffrich*, 2003; *Kaneshima*, 2003] as well as shallow reflections (above 30 km) from the subducted Philippine plate beneath southern Japan [*Weber and Wicks*, 1996]. Notably, our results markedly expand the geographic extent and depth range over which reflectors within the mantle have been observed.

[14] Scatterer locations from the Tonga region agree well with the detection of fast seismic velocities northeast of the Tonga subduction zone (Figure 6 and auxiliary material Figure S3) and are likely related to young subduction along the Vanuatu (New Hebrides) trench [*Jarrard*, 1986; *Hall and Spakman*, 2002]. However, the consistency of this location with the geometry of the Pacific plate subducting beneath the Australian plate [*Fischer et al.*, 1991; *Deal et al.*, 1999; *Tibi and Wiens*, 2005] is not immediately apparent since the scatterer locations are located to the northeast of the Tonga-Fiji subduction zone. Our results, however, are consistent with a ~1000 km long dense slab subducted

since 15 Ma from the Vanuatu subduction zone, oriented toward the northeast, and penetrating into the lower mantle after lying flat in the mantle transition zone over several hundred kilometers: such a geometry can be generated by rapid trench rollback [*Hall and Spakman*, 2002].

[15] Geometrical analysis of the raypaths between sources and *P*P* reflection locations shows that our ability to detect scatterers below Tonga is limited to a volume close to the source. Therefore, the preponderance of detected scatterers in this region is likely related to our source-array geometry and is not necessarily due to an increased scattering potential in this region. Ray-tracing tests show that a minimum distance between the earthquake and the *P*P* scattering point of ~19° is required for a 1000 km deep reflector, while 12° in arc is required to detect a near-source reflector at 670 km depth; shallower scatterers can be imaged at shorter distances. Therefore, we do not expect to detect the dipping Tonga slab in the deep midmantle with this source-receiver combination. The focusing of energy in the first leg of *P*P* from triplications in the wavefield due to the major upper mantle discontinuities [*Wright*, 1972] makes velocity heterogeneities in the upper mantle easier to detect than deeper structures, resulting in a comparatively large number of upper mantle scatterer detections (Figure 7). Possible focusing effects produced by local slab structure can contribute to the large *P*P* amplitudes arising from some deep reflectors.

4. Discussion

[16] A key question involves the origin of the *P*P* precursors that we observe. The most likely origin of the *P*-to-*P* scattered energy with a dominant period of ~1 Hz is
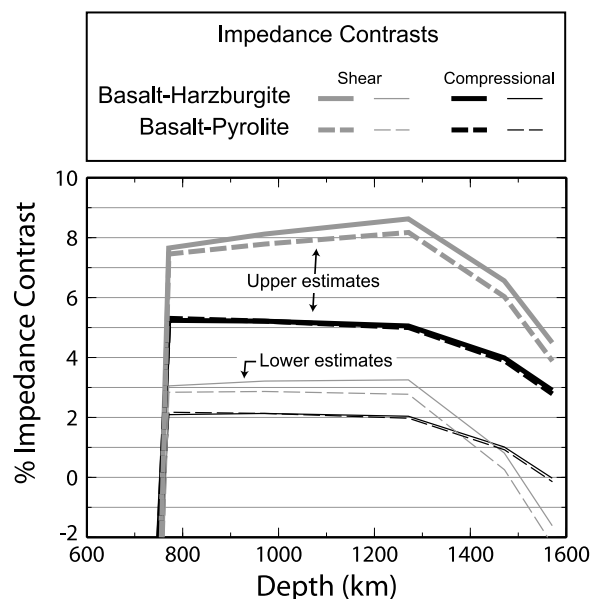
Figure 10. Ranges of possible impedance contrasts between basalt and harzburgite (solid lines) and basalt and pyrolite (dashed lines). Such calculations are particularly sensitive to (1) the controversial bulk modulus of the calcium ferrite structured phase, for which estimates vary from 190 to 243 GPa [*Ono et al.*, 2002; *Guignot and Andrault*, 2004], and (2) the precise pressure derivatives of the shear moduli of the alkalic phases. No thermal contrasts between basalt and underlying or overlying material are included, as local thermal equilibration over the length scale of the reflected wave's sampling is likely to have occurred. The decrease in these contrasts at depths below ∼1300 km is generated by shear softening accompanying the stishovite-$CaCl_2$ phase transition in SiO_2 [*Carpenter et al.*, 2000]. Determining the precise depth extent (as opposed to the absolute amplitude) of this softening is difficult because of the uncertain absolute temperature of the subducted material: the estimate we show is likely an upper bound on the depth range of this shear softening.

scattering from relatively sharp (<10 km thick) gradient zones or discontinuities [*Castle and Creager*, 1999]. Such transitions are too sharp to be produced by the expected temperature gradients associated with subducted material [e.g., *Kincaid and Sacks*, 1997] but rather are likely to be associated with changes in phase and/or composition. Because of the proximity of the scatterer locations to the subducted slabs as imaged in seismic tomography, scatterers may arise from a compositional change related to the presence of ancient subducted posteclogite basaltic crust in the slab juxtaposed with either overlying pyrolitic or underlying harzburgitic material. The mineralogy of subducted basalt differs dramatically from both the Mg silicate perovskite- and magnesiowüstite-dominated pyrolite and harzburgite, with basalt containing nearly 20 wt % free silica (present as stishovite in the shallow lower mantle) and as much as ∼25 wt % of each of $CaSiO_3$ perovskite and an alkalic calcium ferrite-structured and/or so-called NAL (a hexagonal, Al-rich phase of general stoichiometry [K, Na, Ca][Mg, Fe^{II}]$_2$[Si, Al, Fe^{III}, Mg, Fe^{II}]$_6O_{12}$) phases [*Ono et al.*, 2001; *Hirose et al.*, 2005; *Perrillat et al.*, 2006]. We conduct calculations (Figure 10) on a high-pressure basaltic mineralogy from *Ono et al.* [2001] which closely matches that of *Hirose et al.* [2005]. We calculate the ranges of impedance contrast shown in Figure 10 utilizing available elasticity data [*Carpenter et al.*, 2000; *Karki et al.*, 2001; *Ono et al.*, 2002; *Guignot and Andrault*, 2004], third-order Birch-Murnaghan finite strain extrapolations, Reuss averaging [*Watt et al.*, 1976], assumed ranges of Poisson's ratio (which are used to calculate ranges of shear moduli for the Ca ferrite phases) and pressure derivatives of the shear moduli of the alkalic phases that are in the range of those of other lower mantle phases, and comparable average temperature dependences of elastic parameters between the minerals present in high-pressure basalt and those in pyrolite and harzburgite.

[17] Given the uncertainties in elastic parameters at high pressures and temperatures, a wide suite of solutions for compressional and shear impedance contrasts can be constructed with upper and lower bounds illustrated in Figure 10. Much of the variation is associated with uncertainty in the elastic properties of the Ca ferrite-structured phase [*Ono et al.*, 2002; *Guignot and Andrault*, 2004] and particularly the uncertain pressure derivative of its shear modulus; indeed, because of the pressure range of these calculations, uncertainties in the pressure derivatives of the shear moduli of the calcium-rich phases produce far greater uncertainty than the likely range of zero pressure values of its shear modulus. If the calcium-rich phases have comparatively high pressure derivatives of their shear moduli (values of ∼2.5 for dG/dP, where G is the shear modulus, and its pressure derivative is thus unitless), as is calculated to be the case for $CaSiO_3$ perovskite [*Karki et al.*, 2001], then the impedance contrasts are comparatively large; smaller contrasts result if these phases have pressure derivatives of the shear modulus that are more similar to magnesium silicate perovskite and stishovite (near 1.8). The key result of these calculations is that a systematically higher impedance, of between ∼2 and ∼5.5%, is expected between 800 and ∼1300 km depth for compressional waves in posteclogite basalt relative to its overlying (pyrolitic) or underlying (harzburgitic) material. The physical origin of these elevated velocities is straightforward: comparatively low velocity magnesiowüstite in pyrolite and harzburgite is replaced by high-velocity stishovite in basalt, with major uncertainties being associated with the Ca ferrite component. Since the *P* wave impedance contrasts are similar for the changes from basalt-to-harzburgite and basalt-to-pyrolite chemistries, not much information about the nature of the resolved scattering can be gained. Polarities of the *PP* precursors could give some insight into which interface produces the scattering. Unfortunately, as discussed in section 3, the polarities of the precursors vary and hence do not help resolve the issue. The former top of the crust-mantle wedge interface will likely be more disturbed, and probably muted, by the transport of hydrated and silica-rich material across the interface between the crust and overlying mantle by either fluids or magmas [*Prouteau et al.*, 2001]. In effect, metasomatism and low-degree partial melting likely serve not only to deplete the top portion of the subducted crust in silica but also to enrich the overlying mantle, therefore, reducing the impedance contrast between

the former crust and the mantle. It is, therefore, plausible that we detect scattering from the paleo-Mohorovičić discontinuity. Further study of precursors using a larger data set and full waveform modeling will give more constraints that would identify the origin of the $P*P$ arrivals that we observe; indeed, variations in polarity may ultimately prove useful in resolving whether the upper or lower boundary of subducted crustal material is responsible for the observed reflectors. Figure 10 also indicates that shear impedance contrasts are larger than compressional wave contrasts across the interfaces associated with subducted crust; as such, shear wave–associated reflections are also expected to be generated by these reflectors, with their observability naturally depending on the geometry of the reflector and those of available sources and receivers.

[18] These results may provide a means for detecting and tracking slab-associated basaltic material as it travels into Earth's lower mantle. The degree to which former oceanic crust is correlated with broad length-scale tomographically fast features may ultimately provide a means for assessing the structural coherence of the slab as it proceeds to depth. A discrete basalt-harzburgite or basalt-pyrolite interface is anticipated to have significant impedance contrasts throughout much of the depth range of Earth's lower mantle (Figure 10), and depending upon the availability of appropriate source-receiver geometry, the prospect exists for tracking the precise trajectory of the former oceanic crust into the deep mantle. While not uniquely constrained, these results are compatible with the possibility of little or no crustal delamination from the subducting slab (at least at these depths) and that crustal material is advected to lower mantle depths.

[19] Because of the alteration of the basalt-pyrolite interface of the slab during the subduction process, we speculate that the reflectors that we observe are associated predominantly with the paleo-Mohorovičić discontinuity within subducted slabs, i.e., the subducted high-pressure expression of the former Mohorovičić discontinuity. The detections are in good agreement with seismic high velocities in the region as found by seismic P wave and S wave tomography. Since delaminated subducted crust would be below the resolution level of seismic tomography, and tomography is likely most sensitive to the subducted lithospheric part of the slab, the correlation between the reflectors that we detect and tomographic high velocities could indicate, although not constrain, that oceanic crust in the western Pacific might not delaminate from its accompanying lithospheric mantle to depths of at least 1000 km.

5. Conclusions

[20] PP precursors due to scattering at mantle heterogeneities have been successfully used to map geochemical heterogeneities related to subducted crustal material in the upper mantle and midmantle. Using array recordings and high-resolution seismic array methods, we are able to trace subducted material down to depths of ∼1000 km beneath the Tonga and Mariana subduction zones. Mineral physical consideration indicates P wave contrasts of 2.5–5% for high-pressure basalt juxtaposed with pyrolite, which is consistent with that expected to produce reflections. Our calculations show that the S wave impedance contrast is

larger than we expect for P waves and thus the effect of the subducted oceanic crust on the S wavefield might be larger than that observed for P waves.

[21] This study presents data from one medium-aperture array located in northern Canada and, therefore, has limited sampling of the Earth's interior; nevertheless, we have shown that even a single array can image a large number of midmantle features. With improved array and global network coverage, the technique presented here offers a way to globally map small-scale structures below the resolution level of global tomography within the lower mantle. As such, the prospect exists for global seismic imaging at far greater detail than the long-wavelength features of mantle convection; indeed, the fine-scale structures associated with mixing of crustally derived geochemical heterogeneities into the Earth's mantle should ultimately become resolvable.

References

Aki, K., and P. G. Richards (1980), *Quantitative Seismology—Theory and Methods*, Freeman, W.H., San Francisco, Calif.

Capon, J. (1973), Signal processing and frequency-wave number spectrum analysis for a large aperture seismic array, *Methods Comput. Phys.*, *13*, 2–59.

Carpenter, M. A., R. J. Hemley, and H. K. Mao (2000), High-pressure elasticity of stishovite and the P4 (2)/mnm (Pnnm phase transition, *J. Geophys. Res.*, *105*, 10,807–10,816, doi:10.1029/1999JB900419.

Castle, J. C., and K. C. Creager (1999), A steeply dipping discontinuity in the lower mantle beneath Izu-Bonin, *J. Geophys. Res.*, *104*, 7279–7292, doi:10.1029/1999JB900011.

Christensen, U. R., and A. W. Hofmann (1994), Segregation of subducted oceanic crust in the convecting mantle, *J. Geophys. Res.*, *99*, 19,867–19,884, doi:10.1029/93JB03403.

Christensen, U. R., and D. A. Yuen (1984), The interaction of a subducting lithospheric slab with a chemical or phase boundary, *J. Geophys. Res.*, *89*, 4389–4402, doi:10.1029/JB089iB06p04389.

Coltice, N., and Y. Ricard (1999), Geochemical observations and one layer mantle convection, *Earth Planet. Sci. Lett.*, *174*, 125–137, doi:10.1016/S0012-821X(99)00258-7.

Davies, D., E. J. Kelly, and J. R. Filson (1971), VESPA process for analysis of seismic signals, *Nature*, *232*, 8–13.

Deal, M. M., G. Nolet, and R. D. van der Hilst (1999), Slab temperature and thickness from seismic tomography 1. Method and application to Tonga, *J. Geophys. Res.*, *104*, 28,789–28,802, doi:10.1029/1999JB900255.

Earle, P. S. (1999), Polarization of the Earth's teleseismic wavefield, *Geophys. J. Int.*, *139*, 1–8, doi:10.1046/j.1365-246X.1999.00908.x.

Engdahl, E. R. (1995), Imaging of subducted lithosphere beneath South America, *Geophys. Res. Lett.*, *22*, 2317–2321, doi:10.1029/95GL02013.

Fischer, K. M., K. C. Creager, and T. H. Jordan (1991), Mapping the Tonga slab, *J. Geophys. Res.*, *96*, 14,403–14,427, doi:10.1029/90JB02703.

Flanagan, M. P., and P. M. Shearer (1999), A map of topography on the 410-km discontinuity from PP precursors, *Geophys. Res. Lett.*, *26*, 549–552, doi:10.1029/1999GL900036.

Fukao, Y., S. Widiyantoro, and M. Obayashi (2001), Stagnant slabs in the upper and lower mantle transition region, *Rev. Geophys.*, *39*, 291–323, doi:10.1029/1999RG000068.

Gorbatov, A., S. Widiyantoro, Y. Fukao, and E. Gordeev (2000), Signature of remnant slabs in the North Pacific from P wave tomography, *Geophys. J. Int.*, *142*, 27–36, doi:10.1046/j.1365-246x.2000.00122.x.

Grand, S. P. (2002), Mantle shear-wave tomography and the fate of subducted slabs, *Philos. Trans. R. Soc., Ser. A*, *360*, 2475–2491, doi:10.1098/rsta.2002.1077.

Grand, S. P., R. D. van der Hilst, and S. Widiyantoro (1997), Global seismic tomography: A snapshot of convection in the Earth, *GSA Today*, *7*, 1–7.

Gubbins, D., A. Barnicoat, and J. Cann (1994), Seismological constraints on the gabbro-eclogite transition in subducted oceanic crust, *Earth Planet. Sci. Lett.*, *122*, 89–101, doi:10.1016/0012-821X(94)90053-1.

Guignot, N., and D. Andrault (2004), Equations of state of Na-K-Al host phases and implications for MORB density in the lower mantle, *Phys. Earth Planet. Inter.*, *143–144*, 107–128, doi:10.1016/j.pepi.2003.09.014.

Hall, R., and W. Spakman (2002), Subducted slabs beneath the eastern Indonesia-Tonga region: Insights from tomography, *Earth Planet. Sci. Lett.*, *201*, 321–336, doi:10.1016/S0012-821X(02)00705-7.

Hirose, K., N. Takafuji, N. Sata, and Y. Ohishi (2005), Phase transition and density of subducted MORB crust in the lower mantle, *Earth Planet. Sci. Lett.*, *237*, 239–251, doi:10.1016/j.epsl.2005.06.035.

Irifune, T., and A. E. Ringwood (1993), Phase transformations in subducted oceanic crust and buoyancy relationships at depths of 600–800 km in the mantle, *Earth Planet. Sci. Lett.*, *117*, 101–110, doi:10.1016/0012-821X(93)90120-X.

Jarrard, R. D. (1986), Relations among subduction parameters, *Rev. Geophys.*, *24*, 217–284, doi:10.1029/RG024i002p00217.

Kaneshima, S. (2003), Small-scale heterogeneity at the top of the lower mantle around the Mariana slab, *Earth Planet. Sci. Lett.*, *209*, 85–101, doi:10.1016/S0012-821X(03)00048-7.

Kaneshima, S., and G. Helffrich (1999), Dipping low-velocity layer in the mid-lower mantle: Evidence for geochemical heterogeneity, *Science*, *283*, 1888–1891, doi:10.1126/science.283.5409.1888.

Kaneshima, S., and G. Helffrich (2003), Subparallel dipping heterogeneities in the mid-lower mantle, *J. Geophys. Res.*, *108*(B5), 2272, doi:10.1029/2001JB001596.

Kárason, H., and R. D. van der Hilst (2001), Tomographic imaging of the lowermost mantle with differential times of refracted and diffracted core phases (PKP P_{diff}), *J. Geophys. Res.*, *106*, 6569–6588, doi:10.1029/2000JB900380.

Karato, S. I. (1997), On the separation of crustal component from subducted oceanic lithosphere near the 660 km discontinuity, *Phys. Earth Planet. Inter.*, *99*, 103–111, doi:10.1016/S0031-9201(96)03198-6.

Karki, B. B., L. Stixrude, and R. M. Wentzcovitch (2001), High-pressure elastic properties of major materials of Earth's mantle from first principles, *Rev. Geophys.*, *39*, 507–534, doi:10.1029/2000RG000088.

Kennett, B. L. N., and E. R. Engdahl (1991), Traveltimes for global earthquake location and phase identification, *Geophys. J. Int.*, *105*, 429–465, doi:10.1111/j.1365-246X.1991.tb06724.x.

Kincaid, C., and I. S. Sacks (1997), Thermal and dynamical evolution of the upper mantle in subduction zones, *J. Geophys. Res.*, *102*, 12,295–12,316, doi:10.1029/96JB03553.

King, D. W., R. A. W. Haddon, and E. S. Husebye (1975), Precursors to PP, Phys, *Earth Planet. Inter.*, *10*, 103–127, doi:10.1016/0031-9201(75)90029-1.

Krüger, F., M. Baumann, F. Scherbaum, and M. Weber (2001), Midmantle scatterers near the Mariana slab detected with a double array method, *Geophys. Res. Lett.*, *28*, 667–670, doi:10.1029/2000GL011570.

Kubo, T., E. Ohtani, T. Kono, T. Kato, M. Toma, T. Hosoya, A. Sano, T. Kikegawa, and T. Nagase (2002), Metastable garnet in oceanic crust at the top of the lower mantle, *Nature*, *420*, 803–806, doi:10.1038/nature01281.

Lambeck, K., and P. Johnston (1998), The viscosity of the mantle: Evidence from analyses of glacial-rebound phenomena, in *The Earth's Mantle*, edited by I. Jackson, pp. 461–502, Cambridge Univ. Press, New York.

Lay, T. (1994), The fate of descending slabs, *Annu. Rev. Earth Planet. Sci.*, *22*, 33–61, doi:10.1146/annurev.ea.22.050194.000341.

Lee, C. T. A., and W. P. Chen (2007), Possible density segregation of subducted oceanic lithosphere along a weak serpentinite layer and implications for compositional stratification of the Earth's mantle, *Earth Planet. Sci. Lett.*, *255*, 357–366, doi:10.1016/j.epsl.2006.12.022.

Manchee, E. B., and D. H. Weichert (1968), Epicentral uncertainties and detections probabilities from Yellowknife seismic array data, *Bull. Seismol. Soc. Am.*, *58*, 1359–1377.

Meibom, A., and D. L. Anderson (2004), The statistical upper mantle assemblage, *Earth Planet. Sci. Lett.*, *217*, 123–139, doi:10.1016/S0012-821X(03)00573-9.

Miller, M. S., B. L. N. Kennett, and G. S. Lister (2004), Imaging changes in morphology, geometry, and physical properties of the subducting Pacific plate along the Izu-Bonin-Mariana arc, *Earth Planet. Sci. Lett.*, *224*, 363–370, doi:10.1016/j.epsl.2004.05.018.

Muirhead, K. J., and R. Datt (1976), The N-th root process applied to seismic array data, *Geophys. J. R. Astron. Soc.*, *47*, 197–210.

Niu, F. L., H. Kawakatsu, and Y. Fukao (2003), Seismic evidence for a chemical heterogeneity in the midmantle: A strong and slightly dipping seismic reflector beneath the Mariana subduction zone, *J. Geophys. Res.*, *108*(B9), 2419, doi:10.1029/2002JB002384.

Ono, S., E. Ito, and T. Katsura (2001), Mineralogy of subducted basaltic crust (MORB) from 25 to 37 GPa, and chemical heterogeneity of the lower mantle, *Earth Planet. Sci. Lett.*, *190*, 57–63, doi:10.1016/S0012-821X(01)00375-2.

Ono, S., K. Hirose, T. Kikegawa, and Y. Sato (2002), The compressibility of a natural composition calcium ferrite-type aluminous phase to 70 GPa, *Phys. Earth Planet. Inter.*, *131*, 311–318, doi:10.1016/S0031-9201(02)00065-1.

Perrillat, J. P., A. Ricolleau, I. Daniel, G. Fiquet, M. Mezouar, N. Guignot, and H. Cardon (2006), Phase transformation of subducted basaltic crust in the upmost lower mantle, *Phys. Earth Planet. Inter.*, *157*, 139–149, doi:10.1016/j.pepi.2006.04.001.

Prouteau, G., B. Scaillet, M. Pichavant, and R. Maury (2001), Evidence for mantle metasomatism by hydrous silicic melts derived from subducted oceanic crust, *Nature*, *410*, 197–200, doi:10.1038/35065583.

Richards, P. G. (1972), Seismic waves reflected from velocity gradient anomalies in Earth's upper mantle, *Z. Geophys.*, *38*, 517–552.

Ritsema, J., and H. van Heijst (2000), New seismic model of the upper mantle beneath Africa, *Geology*, *28*, 63–66, doi:10.1130/0091-7613(2000)28<63:NSMOTU>2.0.CO;2.

Rost, S., and M. Weber (2002), The upper mantle transition zone discontinuities in the Pacific as determined by short-period array data, *Earth Planet. Sci. Lett.*, *204*, 347–361, doi:10.1016/S0012-821X(02)00999-8.

Rost, S., M. S. Thorne, and E. J. Garnero (2006), Imaging global seismic phase arrivals by stacking array processed short-period data, *Seismol. Res. Lett.*, *77*, 697–707, doi:10.1785/gssrl.77.6.697.

Silver, P. G., R. W. Carlson, and P. Olson (1988), Deep slabs, geochemical heterogeneity, and the large-scale structure of mantle convection—Investigation of an enduring paradox, *Annu. Rev. Earth Planet. Sci.*, *16*, 477–541, doi:10.1146/annurev.ea.16.050188.002401.

Stammler, K. (1993), SeismicHandler: Programmable multichannel data handler for interactive and automatic processing of seismological analyses, *Comput. Geosci.*, *19*, 135–140, doi:10.1016/0098-3004(93)90110-Q.

Tackley, P. J., D. J. Stevenson, G. A. Glatzmaier, and G. Schubert (1993), Effects of an endothermic phase transition at 670 km depth in a spherical model of convection in the Earth's mantle, *Nature*, *361*, 699–704, doi:10.1038/361699a0.

Tibi, R., and D. A. Wiens (2005), Detailed structure and sharpness of upper mantle discontinuities in the Tonga subduction zone from regional broadband arrays, *J. Geophys. Res.*, *110*, B06313, doi:10.1029/2004JB003433.

van der Hilst, R. D., E. R. Engdahl, W. Spakman, and G. Nolet (1991), Tomographic imaging of subducted lithosphere below northwestern Pacific island arcs, *Nature*, *353*, 37–42, doi:10.1038/353037a0.

van der Hilst, R. D., S. Widyantoro, and E. R. Engdahl (1997), Evidence for deep mantle circulation from global tomography, *Nature*, *386*, 578–584, doi:10.1038/386578a0.

van Keken, P. E., E. H. Hauri, and C. J. Ballentine (2002), Mantle mixing: The generation, preservation, and destruction of chemical heterogeneity, *Annu. Rev. Earth Planet. Sci.*, *30*, 493–525, doi:10.1146/annurev.earth.30.091201.141236.

Watt, J. P., and G. F. Davies (1976), The elastic properties of composite materials, *Rev. Geophys.*, *14*, 541–563, doi:10.1029/RG014i004p00541.

Weber, M., and C. W. Wicks (1996), Reflections from a distant subduction zone, *Geophys. Res. Lett.*, *23*, 1453–1456, doi:10.1029/96GL01322.

Wessel, P., and W. H. F. Smith (1998), New, improved version of the generic mapping tools released, *Eos Trans. AGU*, *79*, 579, doi:10.1029/98EO00426.

Workman, R. K., and S. R. Hart (2005), Major and trace element composition of the depleted MORB mantle (DMM), *Earth Planet. Sci. Lett.*, *231*, 53–72, doi:10.1016/j.epsl.2004.12.005.

Wright, C. (1972), Array studies of seismic waves arriving between P and PP in distance range 90(to 115(, *Bull. Seismol. Soc. Am.*, *62*, 385–400.

Wu, R. S., and K. Aki (1988), Seismic wave scattering in three-dimensionally heterogeneous Earth—Introduction, *Pure Appl. Geophys.*, *128*, 1–6, doi:10.1007/BF01772587.

––––––––––––––––––

E. J. Garnero, School of Earth and Space Exploration, Arizona State University, Box 871404, Tempe, AZ 85287-1404, USA.

S. Rost, School of Earth and Environment, Institute of Geophysics and Tectonics, University of Leeds, Leeds LS2 9JT, UK. (s.rost@leeds.ac.uk)

Q. Williams, Department of Earth Sciences, University of California, 1156 High Street, Santa Cruz, CA 95064, USA.